Integrating Materials and Manufacturing Innovation
https://doi.org/10.1007/s40192-021-00209-4

THEMATIC SECTION: METAL ADDITIVE MANUFACTURING MODELING CHALLENGE SERIES 2020

Benchmark Study of Melted Track Geometries in Laser Powder Bed Fusion of Inconel 625

Zhengtao Gan[1] · **Kevontrez K. Jones**[1] · **Ye Lu**[1] · **Wing Kam Liu**[1]

Received: 8 March 2021 / Accepted: 16 April 2021

Abstract
In the Air Force Research Laboratory Additive Manufacturing Challenge Series, melted track geometries for a laser powder bed fusion (L-PBF) process of Inconel 625 were used to challenge and validate computational models predicting melting and solidification behavior. The impact of process parameters upon single-track single-layer, multi-track single-layer, and single-track multi-layer L-PBF processes was studied. To accomplish this, a physics-based thermal-fluid model was developed and calibrated using a proper generalized decomposition surrogate model, then compared against the experimental measurements. The thermal-fluid model was enhanced through the usage of an adaptive mesh and residual heat factor (RHF) model, based on the scanning strategy, for improved efficiency and accuracy. It is found that this calibration approach is not only robust and efficient, but it also enables the thermal-fluid model to make predictions which quantitatively agree well with the experimental measurements. The adaptive mesh provides over a 10-times speedup as compared to a uniform mesh. The RHF model improves predictive accuracy by over 60%, particularly near starting and ending points of the melted tracks, which are greatly affected by the thermal behavior of adjacent tracks. Moreover, the thermal-fluid model is shown to potentially predict lack-of-fusion defects and provide insights into the defect generation process in L-PBF.

Keywords Additive manufacturing · Proper generalized decomposition · Melt pool dynamics · Lack of fusion · Calibration and validation · Ni-based alloy

Introduction

Metal additive manufacturing (AM) produces metallic parts by fusing materials in a layer-by-layer fashion directly from a 3D CAD model [1]. Laser powder bed fusion (L-PBF) is a promising AM process in which a thin layer of metallic powder is spread on a substrate (or the previous layer) and a laser source selectively melts and fuses neighboring powder particles and the previous layer. This is repeated in a layer-by-layer fashion until the desired final part is formed. Since L-PBF has the potential to produce highly customized parts with complex geometries and internal structures, it has garnered great interest from the aerospace, automotive, and biomedical industries [2–4]. Despite offering these advantages and several others, L-PBF is known to struggle with producing parts which have reliable and repeatable mechanical performance due to inconsistencies in the microstructure [5]. However, recent studies prove both the microstructure and mechanical properties of parts produced through AM are significantly influenced by the size and shape of melt pool and resulting solidified track [6].

In L-PBF, the formation of the melt pool is the key to describe the powder/bulk material interactions because it is an intermediate step between solidification and laser source absorption [7]. During the process, localized solid powder is heated up and melted into a liquid after absorbing energy from the passing laser, then cools down and solidifies into a bulk material with a resultant microstructure as the laser moves further away. Porosity in L-PBF may occur due to improper melt pool formation from insufficient melting

Zhengtao Gan and Kevontrez K. Jones have contributed equally to this work.

✉ Zhengtao Gan
zhengtao.gan@northwestern.edu

✉ Wing Kam Liu
w-liu@northwestern.edu

[1] Department of Mechanical Engineering, Northwestern University, Evanston 60208, IL, USA

Published online: 26 May 2021

caused by too little energy absorption or trapped gas caused by vaporization [8, 9]. Much research has shown that energy absorption in L-PBF can be traced through a combination of process parameters such as laser power, scan speed, and spot size. Hence, desired quality of a part fabricated from L-PBF may be achieved through controlling the melt pool by manipulating these processing parameters.

There have been many research efforts aimed at understanding the influence of different AM process parameters and material properties on part quality using computational models and simulations [10, 11]. Using a heat conduction model based on the finite element method is one of the most popular means to model the AM process. For example, Ghosh et al. compared experimentally observed melt pool geometries to computational predictions from a heat conduction model with adequate agreement for various scan speeds and laser powers [12]. However, Yan et al. demonstrated that a thermal-fluid model, which considers fluid flow in the melt pool has greater accuracy of predicting melt pool geometries for a wider range of process parameters than a heat conduction model [13]. Additionally, work performed by Gan et al. used a combination of a heat conduction model, a thermal-fluid model, and a thermal-fluid-vaporization model to demonstrate that the added inclusion of vaporization affects increases predictive accuracy of cooling rates and melt pool geometries even more [14]. Although some computational models have been proven to provide sufficient agreement with experiments, various parameters for the heat source are typically manually calibrated. Additionally, they are usually taken to be constant throughout the entire simulation, which is not physically realistic.

The experiments used to validate and ensure the accuracy of these aforementioned AM process models are required to be well designed and highly controlled. However, high peak temperatures, violent behavior of metallic powder, and the complex multi-physics nature of the melt pool make conducting reliable in situ measurements difficult. Typically, ex situ measurements used for model validation observe the solid/liquid phase boundary at the cross section of fabricated samples [15]. Recently, in situ observation techniques have been proposed to conduct time-resolved measurements for the melt pool depth [16], melt pool visible surface area [17], and cooling rate [18, 19], enabling the design of highly controlled experiments, though in November 2019, the United States Airforce Research Laboratory: Materials & Manufacturing Directorate Structural Materials, Metals Branch (AFRL/RXCM) and America Makes publicly announced the Additive Manufacturing Modeling Challenge Series, which provided a series of highly controlled additive manufacturing challenges for computational models to simulate for opportunities of quantitative validation [20, 21]. Model predictions were submitted by January 31, 2020. Then, all the experimental results were released in January 2021. Through participation in this event, participants were challenged to confidently simulate the L-PBF process with models that they independently developed to provide accurate and efficient predictions. A small amount of experimental data were used for calibration.

This paper describes a computational effort to model one set of the AFRL AM Challenge Series experiments, which measured the geometries of solidified laser tracks left behind by the melt pool for multi-layer and multi-track builds of Inconel 625 (IN625) using the L-PBF process. Hence, the rest of the paper is organized as follows: Sect. 2 briefly describes the experimental methods of the AFRL AM Challenge Series. Section 3 describes the computational methods used to model the experiments in detail. Then, Sect. 4 presents a detailed comparison of the experimental measurements and the computational predictions. Finally, conclusions and key findings of the study are mentioned in Sect. 5.

Experimental Methods

At ARFL, an EOS M280 commercial L-PBF system was used to produce single-layer single-track, single-layer multi-track, and multi-layer single-track (thin-wall) builds of gas-atomized IN625 powder. A Yb-fiber laser with a Gaussian spot size diameter of $4\sigma = 0.1$ mm was used to melt powder layers with a height of 40 µm for all the cases [22]. The atmosphere within the build chamber was supplied purely with Argon gas and build plates were preheated to 353 K. The single-track scans were used for the sake of calibration of the computational models, whereas the multi-track and thin-wall builds were used as the challenge problems. However, both calibration and challenge problems were built on top of AM-printed substrate blocks 5 mm in height. The blocks were rectangular and extended at least 3 mm beyond the end points of the laser scan vectors.

All the single-track laser scans traveled 20 mm from their start position to the their end position, with the laser powers and scan speeds outlined in Table 2, though The multi-track cases had pad sizes of 3 mm × 3 mm, 10 mm × 3 mm, and 15 mm × 3 mm. Additionally, the dwell time between the tracks was 0.5 ms to give the previously melted track time to cool before the subsequent laser scan begins. The full geometries of the multi-track cases are showcased in Fig. 6, and the corresponding laser power and scan speed for each case are shown in Table 3. Contrarily, two thin-wall specimens were built using a unidirectional scanning pattern with a length of 5 mm and a powder layer thickness of 40 µm (10 powder layers) in the build direction. One of the thin walls used a laser power of 300 W and a scan speed of 1230 mm/s, whereas the other used 241 W and 1529 mm/s as shown in Table 5. Since the length of the walls was relatively short, a dwell time of 27 s was used between the deposition of the subsequent

layers. Measurements were taken using a combination of electron backscatter diffraction, to get a top-down description of the track behavior, and optical microscopy on etched cross sections, to measure the track geometries, though a full description of the experimental setup, and measurement procedures can be found in [22].

Computational Models

A framework of integrated computational models was proposed to simulate one set of the AFRL AM Challenge Series experiments in which the Proper Generalized Decomposition (PGD) approach [23, 24] was used to calibrate some unknown parameters of an AM process model. In this work, a thermal-fluid model considering liquid flow inside the melt pool driven by the Marangoni effect was developed as the AM process model to predict the melted track geometries of the L-PBF process, though the key parameters to model the interaction between the metal and the laser heat source were calibrated using a PGD-based surrogate model.

Thermal-Fluid AM Process Model

A well-tested transient three-dimensional thermal-fluid model [11, 14, 25, 26] is used to predict the thermal field in the entire part and velocity field in the melt pool region. To accomplish this, the model solved the governing equations for mass, momentum, and energy conservation given as follows:

$$\frac{\partial \rho}{\partial t} + \frac{\partial \rho u_i}{\partial x_i} = 0 \tag{1}$$

$$\begin{aligned}\frac{\partial \rho u_i}{\partial t} + \frac{\partial \rho u_i u_j}{\partial x_j} &= \frac{\partial}{\partial x_j}(\mu(\frac{\partial u_i}{\partial x_j})) \\ &- \frac{\partial p}{\partial x_i} - \frac{180\mu}{\delta^2}\frac{(1-f_l)^2}{f_l^3 + B}u_i + \rho_{\text{ref}} g_i \beta (T - T_{\text{ref}})\end{aligned} \tag{2}$$

$$\frac{\partial \rho h}{\partial t} + \frac{\partial \rho u_i h}{\partial x_i} = \frac{\partial}{\partial x_i}(k\frac{\partial T}{\partial x_i}) + Q \tag{3}$$

where t is the time, u_i is the ith component of the velocity, μ is the viscosity, p is the pressure, h is the enthalpy, T is the temperature, ρ is the density, k is the thermal conductivity and β is the thermal expansion coefficient. The second component of the acceleration of gravity g_i is $9.8\, m/s^2$ and other components are zero because the direction of the gravity acceleration is vertical.

In this study, μ is set as a constant, δ is the approximate primary dendritic spacing, which is set to 1 μm, B is a small parameter to avoid division by zero and set to 10^{-3}. The relationship between enthalpy and temperature to close the equation set is

$$\rho h = \int_0^T \rho c_p(T')\mathrm{d}T' + \rho L f_l \tag{4}$$

where c_p is the temperature dependent specific heat capacity, L is the latent enthalpy of fusion, and f_l is the volume fraction of the liquid phase.

The heat source from the laser, Q, is described by a cylindrical shape with a Gaussian distribution described below:

$$Q = \begin{cases} \frac{2P\eta}{\pi r_b^2 d}\exp\left(\frac{-2(x^2+y^2)}{r_b^2}\right) & z_{\text{top}} - z \le d \\ 0 & z_{\text{top}} - z > d \end{cases} \tag{5}$$

where P is the laser power, η is the absorptivity, r_b is the laser beam radius, d is the depth of the heat source, and z_{top} is the z-coordinate of the top surface of the computational domain (the original point of the z-coordinate is set to the bottom of the substrate). Although P is a known variable, the other three parameters, i.e., η, r_b, and d, are treated as unknowns and they are highly correlated to the vapor depression phenomenon in the L-PBF process. As reported in the literature [27, 28], as the laser power increases or scan speed decreases, a vapor-induced depression appears and deepens, which leads to higher absorptivity caused by multiple reflections of the laser beam between the liquid/gas interface. Thus, we assume the three parameters, i.e., η, r_b, and d, are related to the ratio between the laser power P and scan speed V, as follows:

$$d = \phi\frac{P}{V} \tag{6a}$$

$$\eta = \max(\xi\frac{P}{V}, 0.28) \tag{6b}$$

$$r_b = \beta\frac{P}{V} \tag{6c}$$

where the coefficients ϕ, ξ, and β are three independent unknowns calibrated using the PGD method described in Sect. 3.2. It is noted that the minimum value of the absorptivity η is constrained to 0.28 [27] during the calibration. The thermal boundary conditions are specified as:

$$q_{\text{ener}} = -h_c(T - T_\infty) - \sigma_s\varepsilon(T^4 - T_{\text{ref}}^4) \tag{7}$$

where h_c is the convective heat transfer coefficient, T_∞ is the ambient temperature, σ_s is the Stefan–Boltzmann constant, ε is the emissivity, and T_{ref} is the reference temperature.

The boundary condition for Eq. (2) at the top surface (assumed to be flat in this study) is:

$$\mu \frac{\partial u_1}{\partial z} = f_l \frac{\mathrm{d}\gamma}{\mathrm{d}T} \frac{\partial T}{\partial x} \tag{8a}$$

$$\mu \frac{\partial u_2}{\partial z} = f_l \frac{\mathrm{d}\gamma}{\mathrm{d}T} \frac{\partial T}{\partial y} \tag{8b}$$

$$u_3 = 0 \tag{8c}$$

where γ is the surface tension, $\frac{\mathrm{d}\gamma}{\mathrm{d}T}$ is the Marangoni coefficient, and u_i is the ith component of the velocity .

The powder layer is treated as a continuous media and it is distinguished from the substrate through its material properties. This is achieved through the use of a consolidated factor, α, defined by the range from 0 to 1. The value of 0 denotes the material is in the original powder state (no consolidation), whereas 1 denotes a bulk state (fully consolidated). As seen from Eq. (9), α is determined by the temperature history, where T_{peak} is the local peak temperature, and T_s and T_l are the material's solidus and liquidus temperatures, respectively. It should be noted that through this definition α solely increases monotonically.

$$\alpha = \frac{T_{\mathrm{peak}} - T_{\mathrm{s}}}{T_l - T_s}. \tag{9}$$

Since α denotes the state of the material at a given time, it is used to determine state-dependent effective material properties. By assuming a linear dependence, the effective material property, λ, is determined by Eq. (10), where λ_{bulk} and $\lambda_{\mathrm{powder}}$ are the appropriate properties for the powder and bulk material, respectively. However, in this work it is assumed this relation only applies to the material's thermal conductivity, specific heat capacity, and density.

$$\lambda = \lambda_{\mathrm{bulk}}\alpha + \lambda_{\mathrm{powder}}(1 - \alpha). \tag{10}$$

The thermo-physical properties of IN625 are summarized in Table 1. As listed in Table 1, the densities at ambient and liquidus temperatures are used for solid and liquid densities, respectively. Values of the bulk density were taken from the literature [29], though for an accurate description of the material's thermal behavior during the L-PBF process, temperature-dependent polynomials were used for the solid's thermal conductivity and solid's specific heat capacity as listed in Table 1. Polynomial coefficients were fitted to previously published experimental measurements [29]. Additionally, a constant convective heat transfer coefficient was used to approximate the low-velocity shield gas flow upon the exposed surfaces.

To consider the transient behavior of the vapor depression caused by localized preheating from adjacent scan paths (i.e., residual heat), we coupled the thermal-fluid model with the residual heat factor (RHF) model proposed by H. Yeung and B. Lane [33]. Since the scan path is composed of discrete points defined by the time step of the simulation and the scan speed of the laser as shown in Fig. 1, the RHF at a specific point (or time step) is defined as

$$\mathrm{RHF_i} = \sum_{k \in S_i} \left(\frac{R - d_{\mathrm{ik}}}{R} \right)^2 \left(\frac{T - t_{\mathrm{ik}}}{T} \right) L_k \tag{11}$$

where the preheating on point i by a previously scanned point k depends on the distance between i and k, denoted as d_{ik}, elapsed time since k was scanned is denoted by t_{ik}, and the normalized laser power at point k is denoted by L_k. The value of L_k is equal to 1 when the laser is on, otherwise it is equal to 0. Threshold values R (0.2×10^{-3} in this case) and T (2×10^{-3} in this case) are used to ignore points which had not interacted with the laser for a sufficient amount of time. The set S_i represents the previous scanned points, i.e., $S_i = \left\{ t_{\mathrm{ik}} < T \cup d_{\mathrm{ik}} < R, \text{where } i > k \right\}$, though this provides a brief introduction, more detailed descriptions of the RHF

Table 1 Thermo-physical properties of IN625 and process constants

Property/parameter	Value	References
Solid density (kg m^{-3})	8440	[29]
Liquid density (kg m^{-3})	7640	[29]
Powder density (kg m^{-3})	4330	[30]
Solidus temperature (K)	1563	[31]
Liquidus temperature (K)	1623	[31]
Solid specific heat capacity (J kg^{-1} K^{-1})	$0.2441T + 338.39$	[30]
Liquid specific heat capacity (J kg^{-1} K^{-1})	709.25	[29]
Powder specific heat capacity (J kg^{-1} K^{-1})	$0.2508T + 357.70$	[30]
Solid thermal conductivity (W m^{-1} K^{-1})	$0.0163T + 4.5847$	[30]
Liquid thermal conductivity (W m^{-1} K^{-1})	30.078	[29]
Powder thermal conductivity (W m^{-1} K^{-1})	0.995	[30]
Latent heat of fusion (kJ kg^{-1} K^{-1})	290	[29]
Dynamic viscosity (Pa s)	7×10^{-3}	[31]
Thermal expansivity (1/K)	5×10^{-5}	[31]
Surface tension (N m^{-1})	1.8	[32]
Marangoni coefficient (N m^{-1} K^{-1})	-3.8×10^{-4}	[32]
Emissivity	0.4	–
Ambient temperature (K)	295	–
Reference temperature (K)	295	–
Preheat temperature (K)	353	–
Convection coefficient (W m^{-2} K^{-1})	10	–
Stefan–Boltzmann constant (W $mm^{-2}K^{-4}$)	5.67×10^{-14}	–

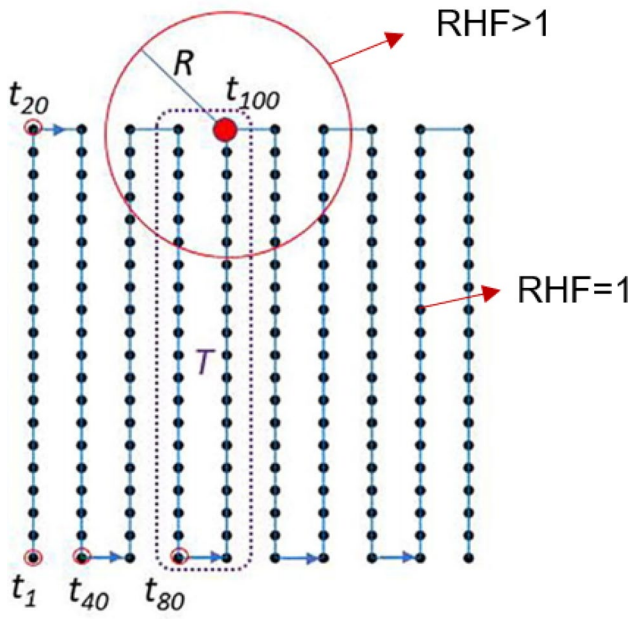

Fig. 1 A schematic of a discrete scan path and the residual heat factor (RHF) [33].

model are provided in reference [33]. However, it should be noted that the RHF can be normalized as $\mathrm{R}HF = \frac{RHF_i}{RHF_c}$ where $\mathrm{R}HF_c$ is equal to the $\mathrm{R}HF_i$ at the middle of the first track. Thus, the RHF is equal to 1 at the middle part of the toolpath, and it is greater than 1 at the corner of the toolpath, as shown in Fig. 1. The heat source parameters can be coupled with the RHF as

$$d = \phi \frac{P}{V} \mathrm{R}HF^2 \tag{12a}$$

$$\eta = \max(\xi \frac{P}{V} \mathrm{R}HF^2, 0.28) \tag{12b}$$

$$r_b = \beta \frac{P}{V} \mathrm{R}HF^2 \tag{12c}$$

where the coefficients ϕ, ξ, β are the independent unknowns calibrated using the PGD method and the exponent of the RHF is an empirical coefficient. This RHF-based heat source is expected to have larger values of η, r_b, and d near starting and ending points of the tracks where the RHF increases.

Proper Generalized Decomposition Method for Model Calibration

Identification of model parameters is a challenging task for AM simulations, especially when the number of unknown parameters becomes important and local minima issues arise. The standard way of handling this problem is to use the genetic algorithm approach [34], in which the computational model is recalled repetitively to evaluate the trial set of parameters. However, this method suffers from an expensive computational cost. Therefore, in our work, we used a powerful PGD-based surrogate modeling approach [23, 24] to handle the model parameter identification (calibration) problem, which has a significantly lower computational cost as compared to the genetic algorithm.

The PGD method used in this work is the Higher-Order PGD (HOPGD)[23, 24], which is designed for non-intrusive data learning and constructing reduced order surrogate models. The basic foundation behind PGD approaches is the separation of variables technique. Considering a d-dimensional function, $f(\mu_1, \mu_2, \ldots, \mu_d)$, which contains the quantity of interest as a function of d parameters, $\mu_i|_{i=1,d} \in \mathcal{D}_i$, the separation of variables results in the following form

$$\begin{aligned} f(\mu_1, \mu_2, \ldots, \mu_d) &\approx f^n(\mu_1, \mu_2, \ldots, \mu_d) \\ &= \sum_{m=1}^{n} F_1^m(\mu_1) F_2^m(\mu_2) \cdots F_d^m(\mu_d), \end{aligned} \tag{13}$$

where f^n is an approximation of f, n is the rank of approximation, and m denotes the m-th mode. Please note that the superscripts n and m do not represent exponential terms. The n-rank approximation f^n is given by the finite sum of products of the separated functions: $F_i^m|_{i=1,d}$, which are a priori unknown and should be obtained either with a precomputed database [23, 24, 35, 36] or by directly resorting to physical models [37–40]. Furthermore, each function F_i^m that represents a variation of the original function f in the parameter direction μ_i is also called a mode function.

The HOPGD relies on the database and falls into the family of data-driven approaches. The database can be either from simulations or experiments. Once obtained, the HOPGD seeks a L^2 projection of data for computing the mode functions $F_i^m|_{i=1,d}$, which can reproduce (or extrapolate) the full parametric function f. Therefore, HOPGD can be used to construct a surrogate model from data for fast prediction. The detailed implementation of the method is presented in [23, 24], and code examples can be found with the GitHub project (https://yelu-git.github.io/hopgd/).

In this work, the parametric melt pool dimension was required to calibrate the heat source model. In particular, the depth and width of the single-track melt pool were the quantities of interest. For identifying the best heat source parameters, it was necessary to know the influence of heat source parameters on the dimension (e.g., the width, W). This relationship can be described by a multidimensional function: $W(p_1, \ldots, p_d)$ with p_i being the parameters we want to identify for the heat source model. Therefore, the PGD form of this function can be written as

$$W(p_1,\dots,p_d) \approx W^n(p_1,\dots,p_d) = \sum_{m=1}^{n} F_1^m(p_1)\cdots F_d^m(p_d), \tag{14}$$

A similar decomposition can be done for the depth of the melt pool: $D(p_1,\dots,p_d)$.

Assuming the parameters $\boldsymbol{p} = [p_1,\dots,p_d]$ belong to a predefined domain $\mathcal{D} = \mathcal{D}_1 \times \cdots \times \mathcal{D}_d$, we want to identify the best $\boldsymbol{p}^*$ s.t.

$$\boldsymbol{p}^* = \arg\min_{\boldsymbol{p}\in\mathcal{D}} \left[J\left(W^{\mathrm{PGD}}, W^e, \boldsymbol{p}\right) + J\left(D^{\mathrm{PGD}}, D^e, \boldsymbol{p}\right)\right] \tag{15}$$

where $W^{\mathrm{PGD}} = W^n$ and $D^{\mathrm{PGD}} = D^n$ are the predictions of the PGD surrogate model, J denotes the objective function which measures the distance between the surrogate model's predictions and the experimental measurements. We repetitively performed the following steps to determine the best parameters:

Step 1. Sample the parameter space $\mathcal{D}$ with the adaptive sparse grid strategy, as described in [24, 41].
Step 2. Compute the melt pool dimension data (W, D) with the AM thermal-fluid model for the selected data points.
Step 3. Use HOPGD and data samples to compute the mode functions in equation (14) and obtain the surrogate model $W^{\mathrm{PGD}}, D^{rmPGD}$.
Step 4. Use the surrogate model to optimize the parameters to match the experimental data. Solve equation (15).

We remark here that the surrogate model used in the above procedure is extremely cheap to evaluate, since the mode functions $F_i^m(p_i)$ are known with data and we only need to perform a 1D interpolation to get the output for a given point $\boldsymbol{p}$. This procedure has been applied to a welding problem and demonstrated great computational efficiency [24]. Thanks to the sparse sampling strategy, the method is applicable to high-dimensional problems at a limited cost. This is usually known as a challenge for other standard surrogate modeling approaches. In what follows, the PGD refers to HOPGD unless otherwise stated.

Results and Discussion

The benchmark study includes three stages as shown in Fig. 2: (1) eleven single-track experiments with various laser powers and scan speeds were used to calibrate unknown parameters in our computational thermal-fluid model, (2) six multi-track and two multi-layer simulations with different toolpaths and process parameters were conducted using the calibrated computational model, and (3) the geometrical information of melted tracks and layers was extracted from the simulations and compared with experimental measurements for assessing the predictive capability of the computational model.

Model Calibration Using Single Tracks

The experimental data provided for calibration is based on single-track results of eleven cases. The processing conditions and the corresponding melt pool geometric descriptions are depicted in Table 2. Since there are eleven cases for each quantity, we group them into two vectors: $\boldsymbol{W}^e = [W_1^e,\dots,W_{11}^e]$, $\boldsymbol{D}^e = [D_1^e,\dots,D_{11}^e]$ to denote the widths and the depths, respectively. Here, we only consider the mean value of each case. The deviation data will be considered by the weight coefficients used in the objective function and will be clarified later.

Note that each width corresponds to the Top-Down Width of the released data [30], and each depth corresponds to Cross section Depth plus Cross section Height [30]. The Original Depth is the data released before the AFRL AM Challenge Series results were announced, and unfortunately it was discovered that this dataset contained some mislabeled (i.e., incorrect) data points. The Corrected Depth is the corrected data released by AFRL after the results were announced. It should be noted that, the widths remain unchanged.

For calibrating our computational model, the PGD-based surrogate model is constructed for three heat source related parameters (see Eq. ()): ξ, β, ϕ. In this case, we can consider a tensor form of Eq. (14), which reads

$$\boldsymbol{W}^{\mathrm{PGD}}(\xi,\beta,\phi) = \sum_{m=1}^{n} \boldsymbol{F}_1^m(\xi) \otimes \boldsymbol{F}_2^m(\beta) \otimes \boldsymbol{F}_2^m(\phi) \tag{16}$$

and,

$$\boldsymbol{D}^{\mathrm{PGD}}(\xi,\beta,\phi) = \sum_{m=1}^{n} \tilde{\boldsymbol{F}}_1^m(\xi) \otimes \tilde{\boldsymbol{F}}_2^m(\beta) \otimes \tilde{\boldsymbol{F}}_2^m(\phi). \tag{17}$$

As explained in Sect. 3.2, the PGD model is used to minimize the objective function below

$$\begin{aligned} J =& J\left(\boldsymbol{W}^{\mathrm{PGD}}, \boldsymbol{W}^e, \xi, \beta, \phi\right) + J\left(\boldsymbol{D}^{\mathrm{PGD}}, \boldsymbol{D}^e, \xi, \beta, \phi\right) \\ =& \sum_{i=1}^{11} w_i \| W_i^{\mathrm{PGD}}(\xi,\beta,\phi) \\ & - W_i^e \| + \sum_{i=1}^{11} \tilde{w}_i \| D_i^{\mathrm{PGD}}(\xi,\beta,\phi) - D_i^e \| \end{aligned} \tag{18}$$

where the weight coefficients $w_i|_{i=1,11}$ with the property of $\sum_i w_i = 1$ are used to consider the deviation data. This basically means the larger the deviation is, the smaller the weight coefficient will be.

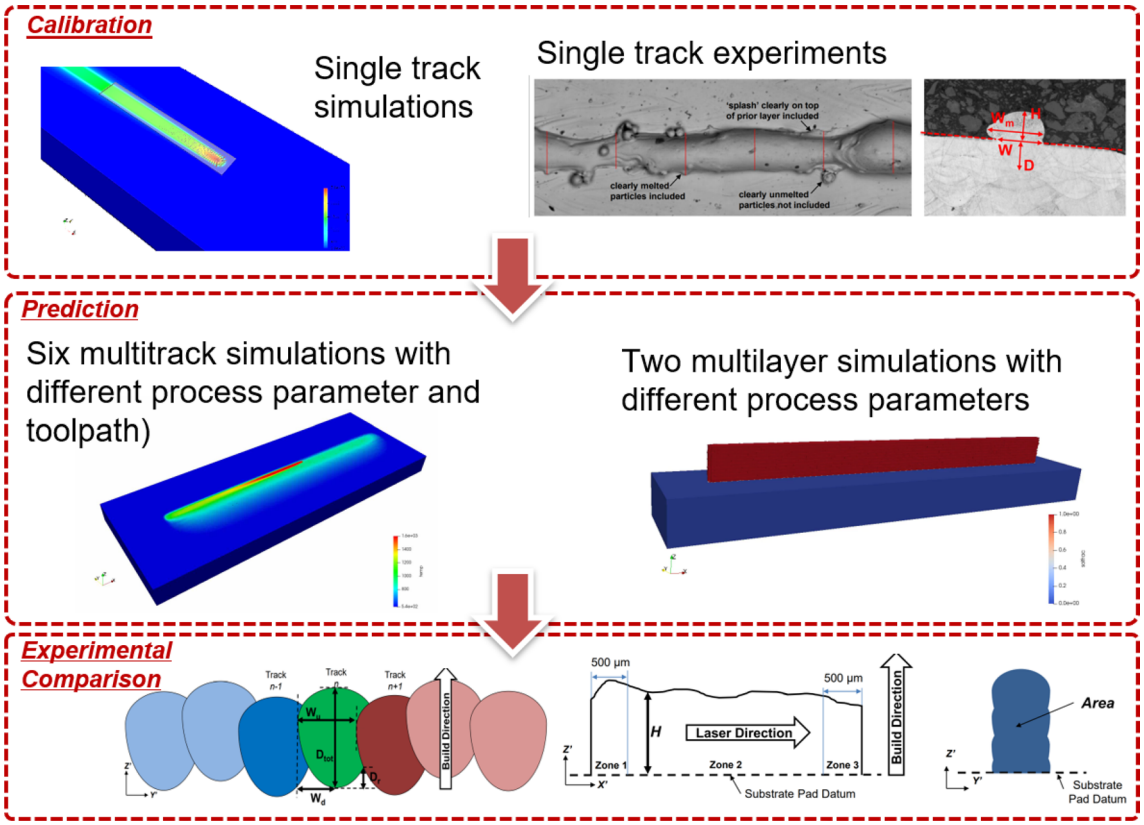

Fig. 2 A schematic of this benchmark study including three stages: calibration, prediction, and experimental comparison. Experimental data and figures are provided by Air Force Research Laboratory (AFRL) Additive Manufacturing (AM) Modeling Challenge Series: Challenge 2 (https://materials-data-facility.github.io/MID3AS-AM-Challenge/).

Table 2 Experimental data for single-track cases

Case number	Laser power (W)	Scan speed (mm/s)	Width (μm)	Original depth (μm)	Corrected depth (μm)
1 (B10)	300	1230	112.0 ± 11.1	89.1 ± 23.7	113.4 ± 21.3
2 (B11)	300	1230	112.0 ± 11.9	87.2 ± 21.0	118.0 ± 30.8
3 (B12)	290	953	127.6 ± 7.0	141.9 ± 23.1	140.1 ± 16.6
4 (B13)	370	1230	122.9 ± 8.4	140.1 ± 16.6	141.9 ± 23.1
5 (B14)	225	1230	96.0 ± 13.9	118.0 ± 30.8	85.3 ± 21.0
6 (B15)	290	1588	97.9 ± 14.0	113.4 ± 21.3	89.1 ± 23.7
7 (B16)	241	990	112.0 ± 13.0	103.7 ± 18.5	103.7 ± 18.5
8 (B17)	349	1430	110.7 ± 11.3	118.6 ± 20.5	118.6 ± 20.5
9 (B18)	300	1230	112.7 ± 12.7	115.7 ± 35.2	115.7 ± 35.2
10 (B19)	349	1058	129.9 ± 7.0	147.5 ± 26.7	147.5 ± 26.7
11 (B20)	241	1529	89.3 ± 12.8	76.4 ± 25.2	76.4 ± 25.2

For the AFRL AM challenge problems, we used the original data of widths and depths for the calibration. The range of the three parameters is set to be $\mathcal{D}_\xi := [1,\ 2.5] \times 10^{-3}$, $\mathcal{D}_\beta := [1.3,\ 2.0] \times 10^{-7}$, $\mathcal{D}_\phi := [3.8,\ 4.5] \times 10^{-7}$. These choices were made to ensure the resulting heat source parameters remained at a reasonable level for all of the eleven cases. Concerning the computational cost, the total number of simulation data for constructing the PGD model is 17. Each of them contains the melt pool dimensions of the eleven cases and only takes about 20 minutes to compute. The online optimization cost takes less than 1 minute. The final results obtained by the calibrated parameters are depicted in Fig. 3. The main discrepancy is observed in the depth data, especially for cases 5 and 6, which is due to the

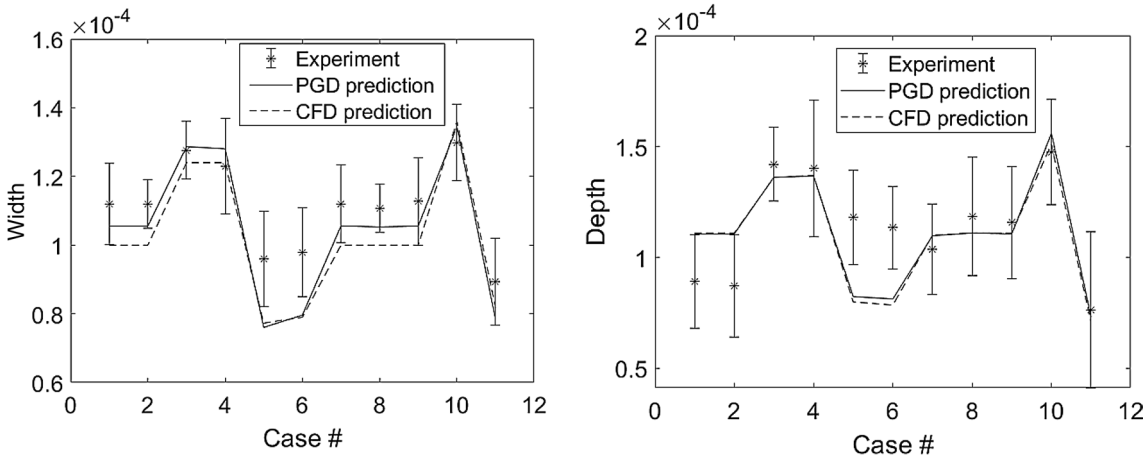

Fig. 3 Calibration result with PGD and the original experimental data. Width (m) and depth (m) against case number. CFD prediction is given by the original thermal-fluid model with the calibrated parameters, and has shown a good agreement with the PGD prediction

mislabeled (incorrect) experimental data points included in the original experimental dataset.

In the post-challenge phase, the depth data was corrected in newly released results. Therefore, we have repeated the calibration using the corrected data (see Fig. 4). The final calibrated values for the three parameters remain the same as previously and agree more favorably with the experiments, which means the right parameters had already been found even with the original dataset which included a few incorrect data points. This demonstrates the robustness of the PGD-based calibration strategy [23, 24]. Hence, we can confirm that the new corrected data would not affect our multi-track or multi-layer predictions, which were conducted based on the original calibrated parameters.

As shown in Fig. 5, the eleven corrected calibration data cases and corresponding simulation results are organized according to the heat input, i.e., laser power P divided by scan speed V, as the x-axis. The single-track melt pool depths and widths are proportional to the heat input and the calibrated model can accurately capture these trends.

Prediction and Validation of Multi-Track Scans

We conducted six multi-layer simulations with various process conditions using the calibrated model (with known heat source coefficients ϕ, ξ, β) to predict geometrical details of the melted tracks for the L-PBF process. The substrate geometries and toolpaths of those six simulations (B26, B27, B31, B34, B35, and B38) are shown in Fig. 6. The toolpaths are labeled according to the L-PBF experiments performed by AFRL. The black frames show the substrate dimensions, and the arrows represent the laser scan paths. Similar to the experiments, when the beam reaches the end of a scan path, there is a 0.5 ms period during which the laser beam is

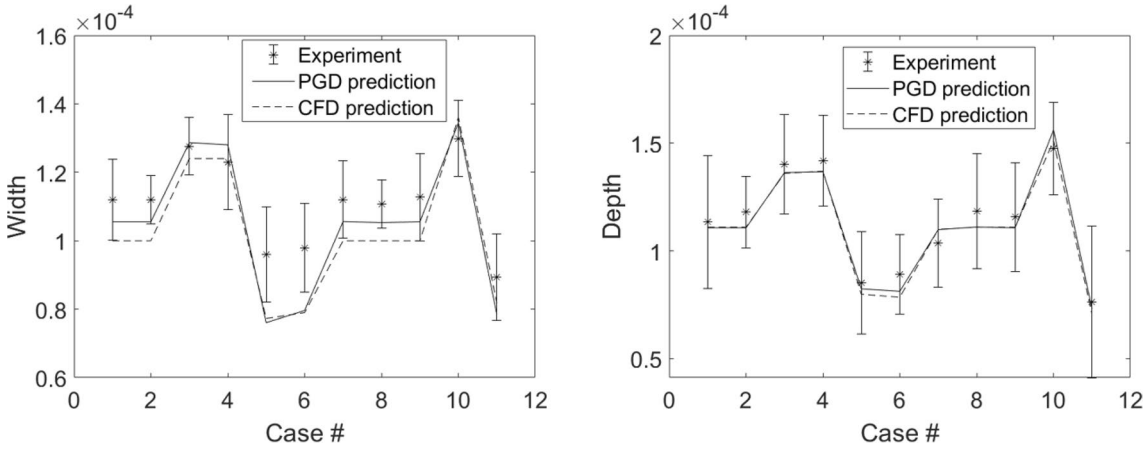

Fig. 4 Calibration results with PGD and the corrected experimental data. Width (m) and depth (m) against case number. CFD prediction is given by the original thermal-fluid model with the calibrated parameters, and has shown a good agreement with the PGD prediction

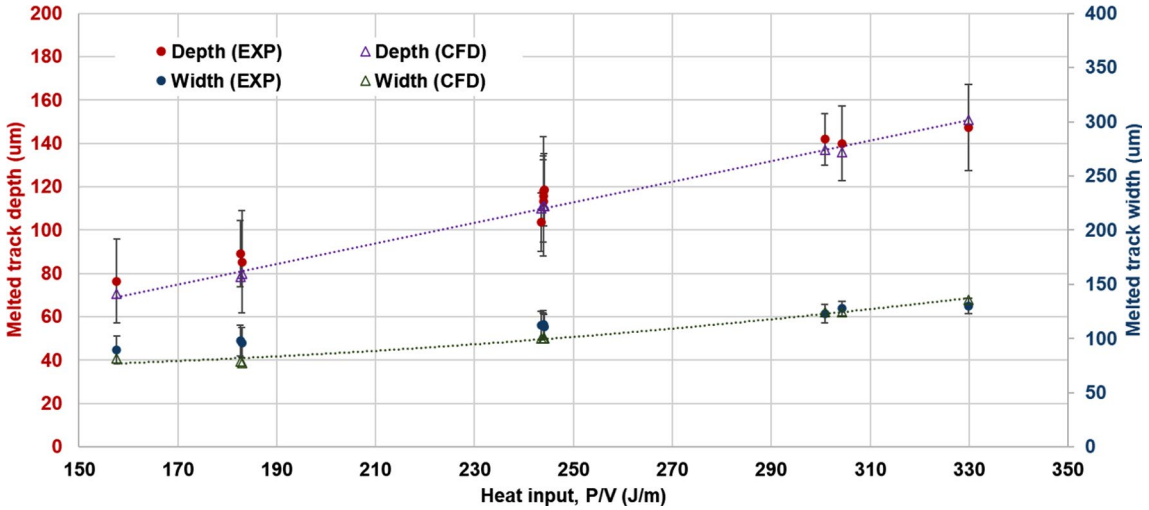

Fig. 5 Reorganized calibration results based on the corrected experimental data. The heat input, i.e., laser power P divided by scan speed V, is used as the x-axis. The red solid markers represent the melted track depth. The blue solid markers represent the melted track width. The hollow markers represent calibrated simulation results. Two dashed lines indicate the trends of the simulation results

turned off while the beam moves to the beginning position of the next scan path. It should be noted that case B35 has a different scan pattern from the others. A 1 mm length block is built first and then a larger block with a 9 mm length is built. Three cases, i.e., B27, B31, and B34, have identical dimensions of substrates and toolpaths but different process parameters. The process parameters used for all six cases are summarized in Table 3.

First, we present the results of case B26. An adaptive mesh system was designed to accelerate the computation by only refining the mesh region near the melt pool. This fine mesh region follows the laser scan. Figure 7 presents temperature fields and corresponding mesh systems at three different tracks: the first track (Fig. 7a, d), 15th track (Fig. 7b, e), and 30th track (Fig. 7c, f). A fine mesh region with a mesh size of $20 \times 5 \times 5$ µm (Fig. 7g) moves along the y-direction, which is perpendicular with the laser scan direction, i.e., x-direction. The design of the adaptive mesh was inspired by the work done by Mukherjee et al. [42].

We coupled fluid dynamics in the melt pool with heat transfer during the process, which can significantly improve the prediction accuracy of melt pool geometry and temperature field near the high thermal gradient region [14]. Figure 8 shows a melt pool profile and velocity field inside at the middle of the 15th track of case B26. The Marangoni effect leads to a surface tension-driven flow in the melt pool. The maximum velocity in the melt pool is around 2000 mm/s, which affects the melt pool geometry and solidification cooling rate.

We created a variable, solidID, to record the melted region at each track as shown in Fig. 9. The original substrate and powder layer are assigned to be zero value of the solidID. If the temperature at a specific cell is higher than the solidus temperature during the i^{th} track of laser scan, the solidID of it will be assigned to i, and i is from 1 to 30 for case B26 because it has a total number of 30 tracks. Figure 9 also shows three cross sections at different positions in the x-direction, which present the cross-sectioned melted areas. It is noted that the original point of the x-direction ($x' = 0$ mm) is the starting point of the laser scan. Cross section A–A ($x' = 0.1$ mm) is close to the starting point of the toolpath, cross section B–B ($x' = 1.5$ mm) is at the middle of the toolpath, and cross section C–C ($x' = 2.9$ mm) is close to the ending point.

These cross-sectioned melted areas are useful because they can be compared with experimental observations by optical microscope or scanning electron microscope. Figure 10 shows the comparison of melted tracks between the computational results and experimental measurements at two cross sections, A–A and B–B, of case B26. The simulations predict the geometrical pattern and size of the fusion boundary (highlighted by black lines) at the two cross sections of case B26: cross section A–A that is close to the starting point and the cross section B–B at the middle of the toolpath. With the assumption of the flat top surface in the model, the free surfaces of the melted tracks in the experiments are not considered in this study. It can be seen that first melted track (at left-most) is smaller than the others because the first track scans on a room-temperature substrate while the subsequent laser tracks, after the first, scan with a heated substrate. Residual heat transfers from the preceding laser scans to the substrate, which generates a larger melt pool and resulting melted track. Another interesting fact shown in Fig. 10 is that, at the A–A cross

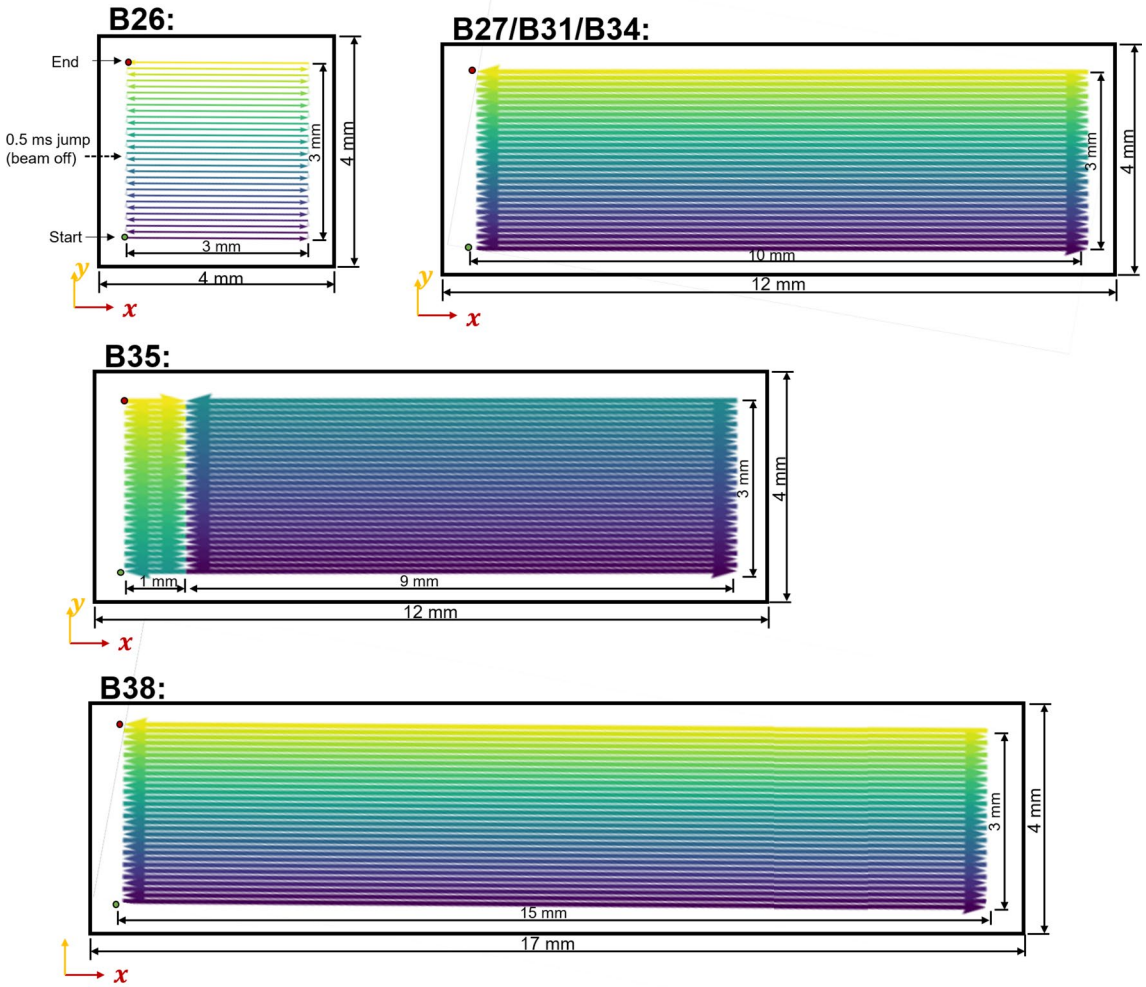

Fig. 6 Substrate geometries and toolpaths of the six simulations (B26, 27, B31, B34, B35, and B38). The start point is marked as a green dot and the ending point is marked as a red dot. The arrows represent the scan paths of the laser. The color associated with those arrows represents the order of the toolpath. The violet arrow is the first track and the yellow one is the last track

Table 3 Process parameters used for multi-track cases

Case number	Laser power (W)	Scan speed (mm/s)	Hatch spacing (mm)	Toolpath plane dimensions (mm)	The number of tracks
B26	300	1230	0.1	3 × 3	30
B27	300	1230	0.1	10 × 3	30
B31	300	1230	0.075	10 × 3	30
B34	300	1230	0.125	10 × 3	30
B35	300	1230	0.1	10 × 3	60
B38	290	953	0.1	15 × 3	30

section, the melted tracks of odd-numbered laser scans (except the first scan) are deeper and wider than those of the even-numbered scans. However, at the B–B cross section the melted tracks of odd- and even-numbered scans have similar size and shape. This difference only appears near the starting and ending points of the laser scans where the melt pool is hotter, deeper, and wider due to residual heat generated by the previous scan.

To illustrate this transient behavior at the starting and ending regions of the toolpath, Fig. 11 presents the evolution of the melt pool represented by red isotherms of the solidus temperature at different times for which the laser traverses

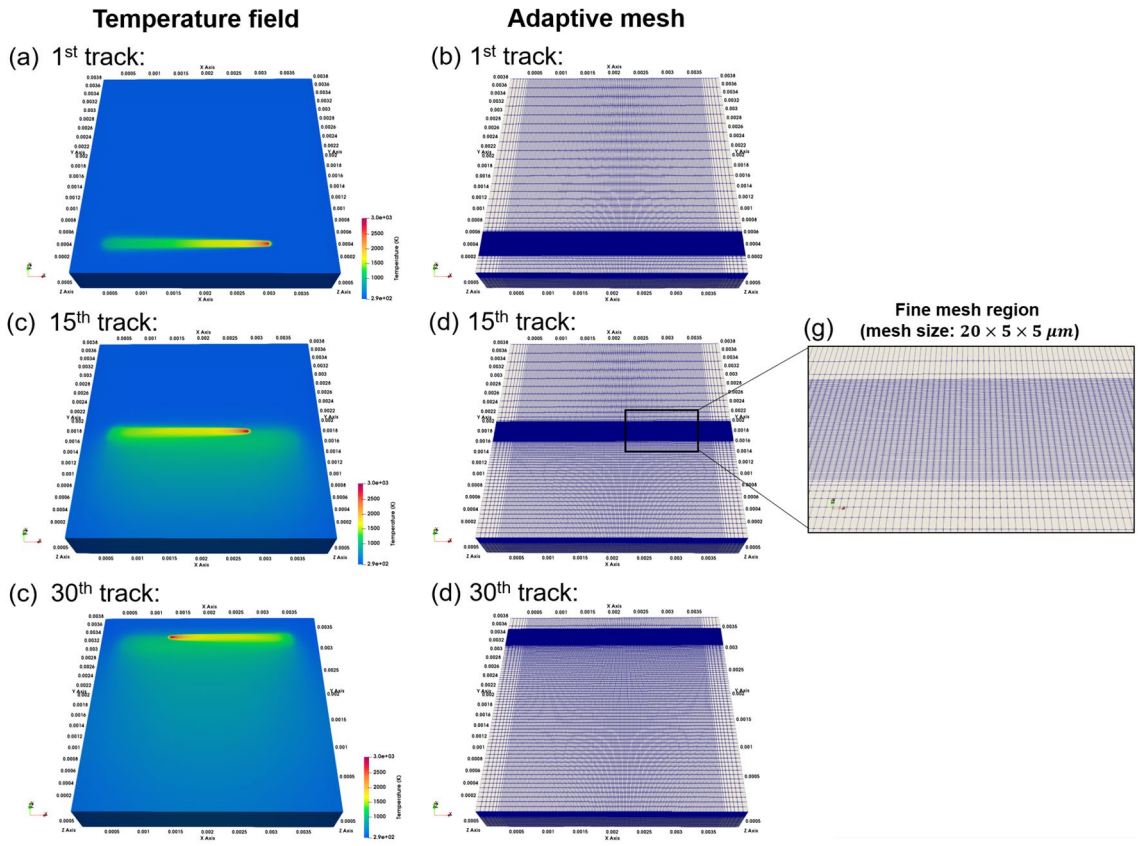

Fig. 7 Predicted temperature fields at different tracks and corresponding adaptive mesh systems for case B26. **a** Predicted temperature field for the 1st track. **b** Adaptive mesh system at the 1st track. **c** Predicted temperature field for the 15th track. **d** Adaptive mesh system at the 15th track. **d** Predicted temperature field for the 30th track. **f** Adaptive mesh system at the 30th track. **g** magnification view of fine mesh region at the 15th track

the first and second tracks. The peak temperature, depth, and width of the melt pool at each time are also marked. At the end of the first track as shown in Fig. 11a, the melt pool is well developed and reaches a steady state in which the size and shape of the melt pool are approximately unchanged in time. Since there is a 0.5 ms dwell time between the two tracks, the melt pool shrinks quickly while the laser is turned off as shown in Fig. 11b. However, the 0.5 ms dwell time is not long enough to cool down the whole melt pool. When the beam is on at the starting point of the second track, the melt pool generated by the first scan still exists, which leads to a new melt pool with a higher peak temperature generated at the hot substrate as shown in Fig. 11c, d. The high peak temperature inside the melt pool could result in stronger recoil pressure and form a deeper vapor depression that increases the thermal energy input by multiple reflection of the laser beam [27]. An experimental study captured the similar phenomenon using X-ray imaging technique is reported in reference [43]. When the laser moves away from the starting point, the size and peak temperature gradually decrease until the melt pool reaches a steady state (Fig. 11e, f).

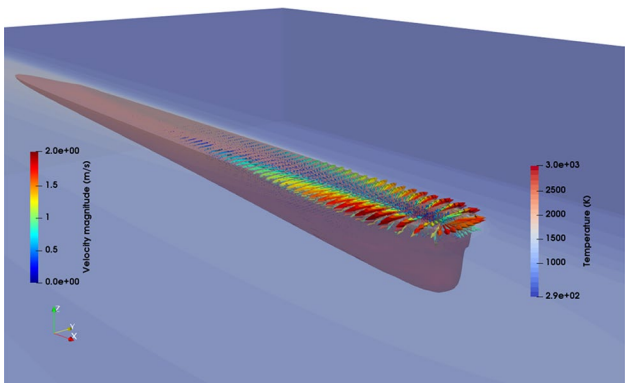

Fig. 8 Melt pool profile and velocity field in the melt pool at the middle of the 15th track of case B26. A red isotherm at solidus temperature represents the melt pool boundary. Arrows indicate velocity of liquid metal and are colored by velocity magnitude. Temperature is also shown as the color legend

To consider these transient dynamics and accurately predict the melt pool dimensions at the transient regions of the

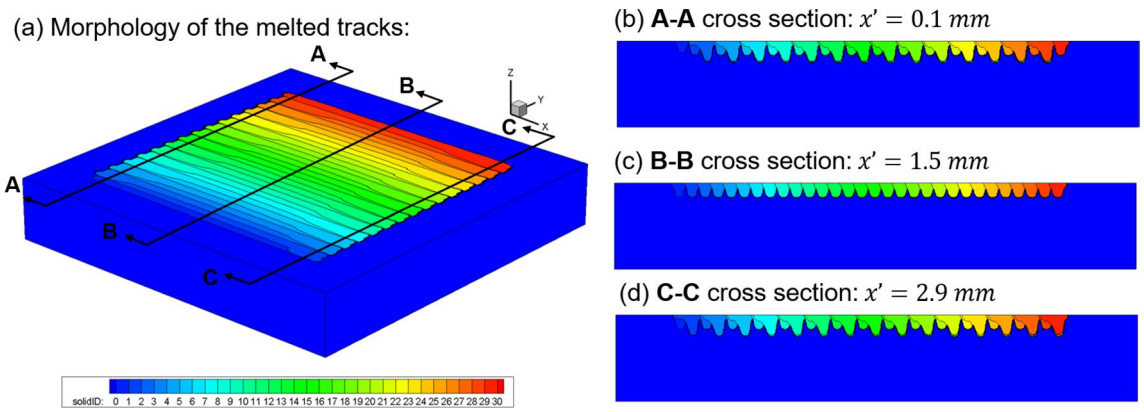

Fig. 9 Morphology of the melted tracks described by the solidID. **a** Three-dimensional view of the substrate and melted tracks. Three positions of cross sections are also marked. **b** A–A cross section at $x' = 0.1$ mm ($x' = 0$ mm indicates the starting point of the toolpath in x-direction). **c** B–B cross section at $x' = 1.5$ mm. **d** C–C cross section at $x' = 2.9$ mm

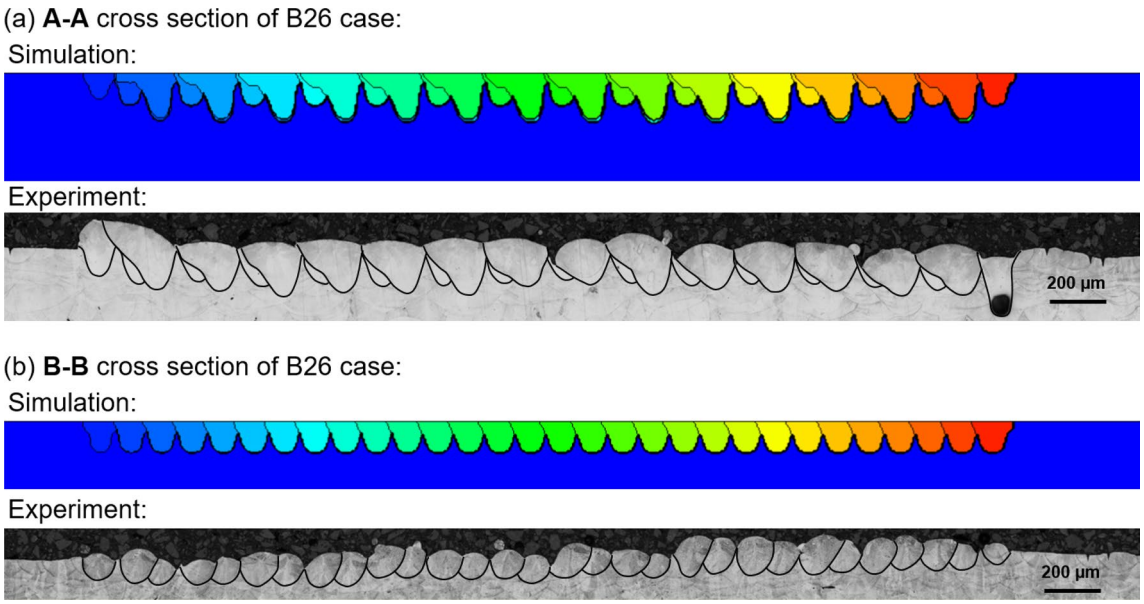

Fig. 10 Comparison of melted track geometries between simulation and experimental measurement. **a** A–A cross section of case B26 **b** B–B cross section of case B26

toolpath, we coupled the thermal-fluid model with a residual heat factor (RHF) model as described in Section 3.1. Figure 12 shows quantitative comparisons of melted track geometries between experiments and two computational models with and without considering the RHF. The definitions of the melted track geometries, i.e., D_{tot}, D_r, W_d, and W_u, are provided in Fig. 13 and the caption of Fig. 12. More detailed definitions are provided in reference [22]. For each case, tracks are numbered from 1 to N, where 1 is the first track deposited, and N is the last. In all cases, measurements of the four quantities mentioned above begin on track 4, and end on track N-3 (i.e., ignoring the first three and last three). The average and standard deviation of each quantity for the even- and odd-numbered tracks are plotted in Fig. 12. The error bar represents the standard deviation. The model predictions with RHF (green bars) match the experiments (blue bars) quite well at both the middle ($x' = 1.5$ mm) and beginning ($x' = 0.1$ mm) of the toolpath. However, if the RHF is ignored in the model (i.e., the model without RHF), the melted track size is underestimated for the odd-numbered scans at the beginning of the toolpath ($x' = 0.1$ mm). That is because, by coupling with the RHF, the thermal-fluid model considers adaptive heat source depth and absorptivity, which increase when the laser creates a new track. Similar

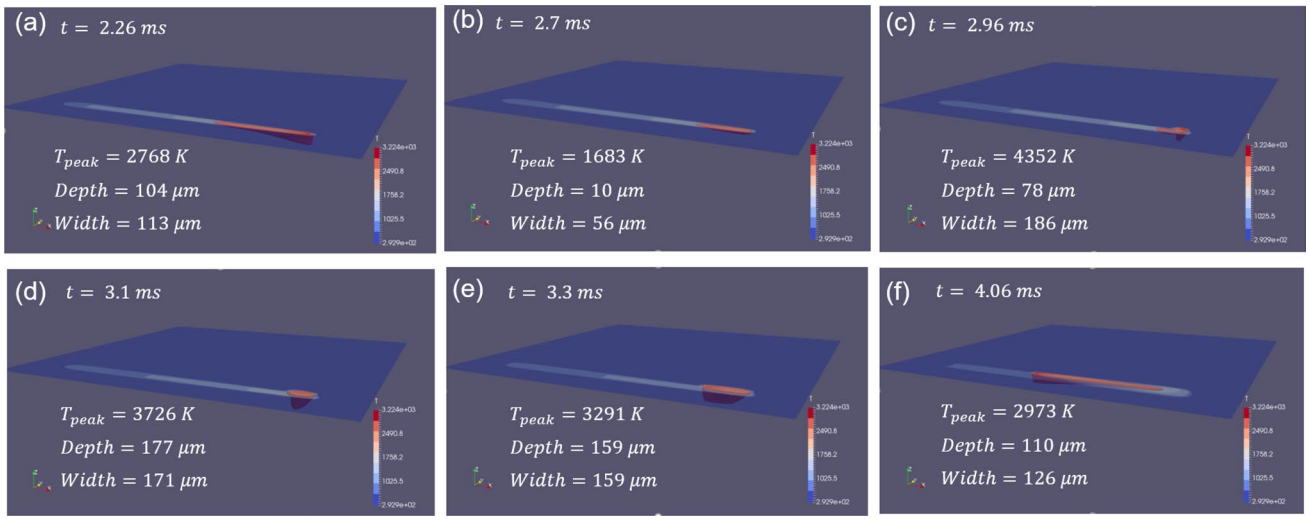

Fig. 11 Evolution of melt pool for the first and second scans of case B26. The melt pool dimensions and its peak temperature are also marked. **a** $t = 2.26$ ms. **b** $t = 2.7$ ms. **c** $t = 2.96$ ms. **d** $t = 3.1$ ms **e** $t = 3.3$ ms **f** $t = 4.06$ ms

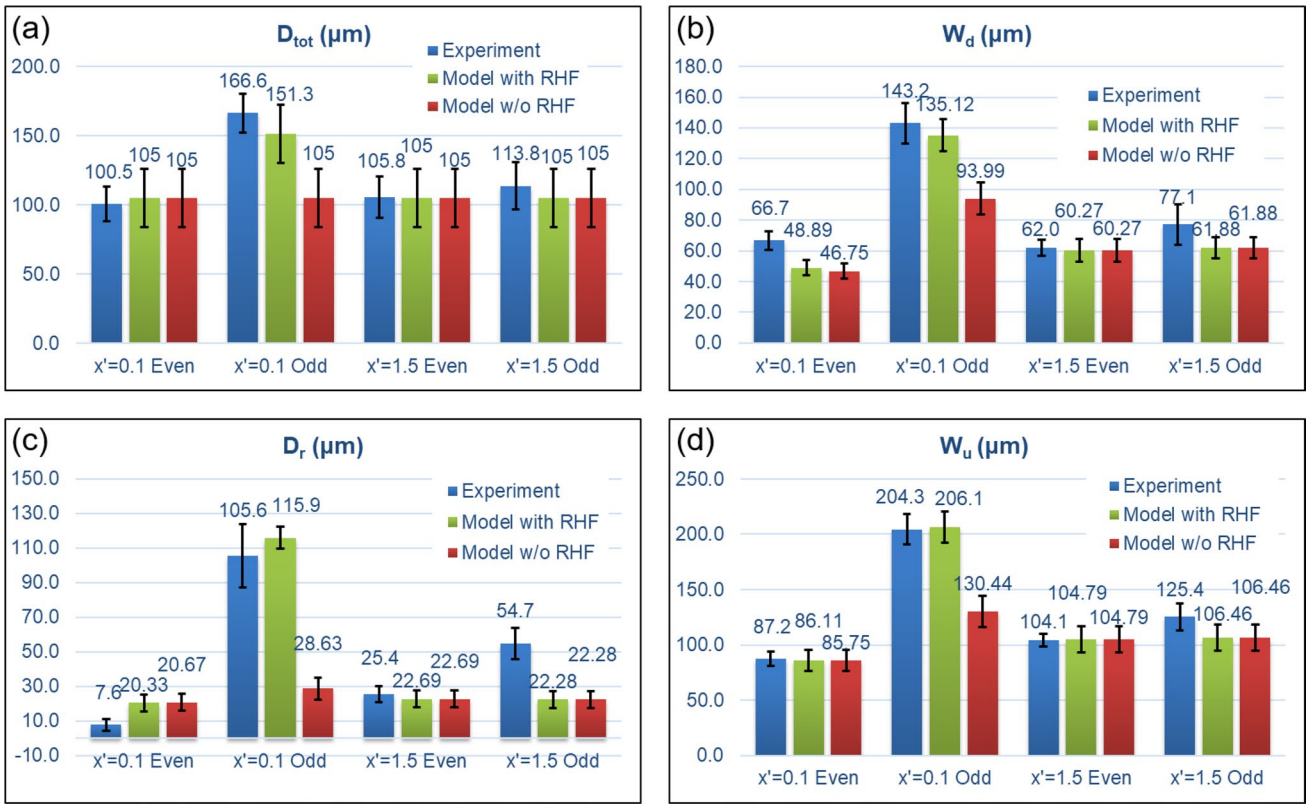

Fig. 12 Quantitative comparisons of four melted track dimensions between experimental measurements and model predictions with and without residual heat factor (RHF). **a** Distance D_{tot} measured along the vertical direction from lowest to highest points of a melted track. **b** Distance W_d measured along the horizontal direction from the lowest portion of a track in the vertical direction to the lowest value in the horizontal coordinate of the track. **c** Distance D_r measured along the vertical direction from the lowest point of a track in the vertical direction, to the intersection of melted track boundaries for the track with the subsequent track. If there is no intersection with an adjacent track, set $D_r = D_{tot}$ for that track. **d** Distance W_u measured along the horizontal direction extending from the lowest horizontal coordinate for any part of a track to the lowest horizontal value along the interface between the track and the next subsequent track. In case there is no overlap with a subsequent track, record the distance from the lowest to the highest horizontal value for the track. An illustration including these distances is provided in Fig. 13

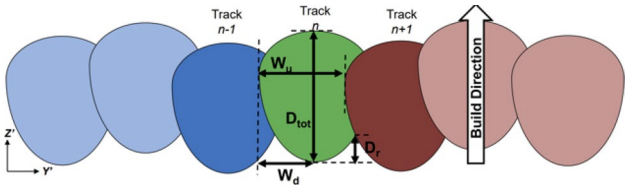

Fig. 13 Schematic of a measurement plane with desired measurements [30]

phenomenon appears for other multi-track cases (i.e., B27, B31, B34, B35, and B38). The quantitative comparisons of melted track geometries for those cases are provided in Supplementary Figs. 1 to 5.

More interestingly, the developed model can predict lack-of-fusion patterns in the L-PBF process. Lack of fusion, where there is no complete adherence of the current melt to the surrounding part, is a type of AM process-induced defect that has a negative influence on as-built mechanical properties. It is caused by insufficient energy input that cannot create a large enough overlapping region between two adjacent tracks [44]. Figure 14a shows the predicted lack-of-fusion patterns for case B35. The toolpath of this case is provided in Fig. 6. As shown in Fig. 14a, the color legend indicates the density field after the L-PBF process. The minimum value (illustrated as blue) is the effective powder density ($4300 \mathrm{kg}/m^3$) and the maximum value (illustrated as red) is the solid material density ($8400 \mathrm{kg}/m^3$). The top layer is originally assigned as the effective powder density. During the L-PBF process, if the peak temperature of a spatial point is higher than the solidus temperature, the density of this point will be updated that of the liquid. After the temperature drops down to solidus temperature, the density is converted to that of the bulk solid, which is much higher than the effective powder density. The values of those densities are provided in Table 1.

During this process, a few powders between two laser scanned tracks might remain unmelted if the energy input from the laser is insufficient to create a large enough melt pool. Those small regions become lack of fusion after the toolpath is complete. For example, Fig. 14b shows a few unmelted powders and open pores between the laser scans reported in reference [45]. Our model can predict the lack-of-fusion regions (small blue dots in Fig. 14a) between laser

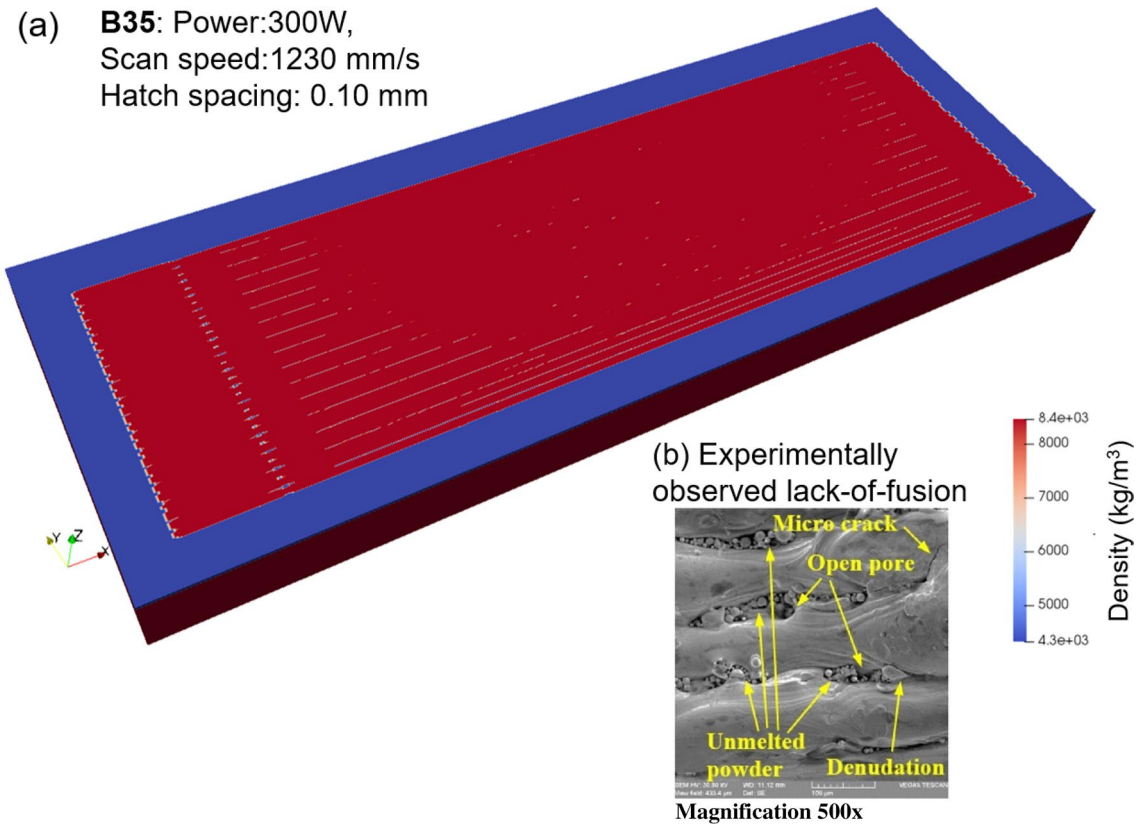

Fig. 14 Lack-of-fusion pattern for case B35: **a** predicted density field after laser scanning presenting the lack-of-fusion pattern. The color legend indicates the density at spatial points. The blue represents the effective powder density ($4300 \mathrm{kg}/m^3$) and the red represents the solid material density ($8400 \mathrm{kg}/m^3$). **b** Experimentally observed lack of fusion from the top view reported in reference [45]

scanned tracks and toolpath blocks. The pattern of the lack of fusion depends on toolpath strategy and process parameters. The developed model is a potential effective tool to optimize the process parameters for mitigating or eliminating the lack-of-fusion defect. For example, Fig. 15 shows predicted lack-of-fusion patterns for three cases: B27, B31, and B34. These cases have the same toolpath pattern and process parameters except for the hatch spacing. The hatch spacing of the three cases is 0.125 mm, 0.1 mm, and 0.075 mm, respectively. It can be clearly seen that decreasing hatch spacing from 0.125 mm to 0.075 mm mitigates the lack-of-fusion defect in the L-PBF, which demonstrates the effectiveness of our model as a process optimizer for the L-PBF process.

Table 4 lists computational parameters and computational time for all six multi-track cases. Two mesh systems, i.e., uniform mesh and adaptive mesh systems, are compared for each case. It can be seen from the last column of Table 4, the adaptive mesh system can significantly reduce the computational time by decreasing the number of cells required and

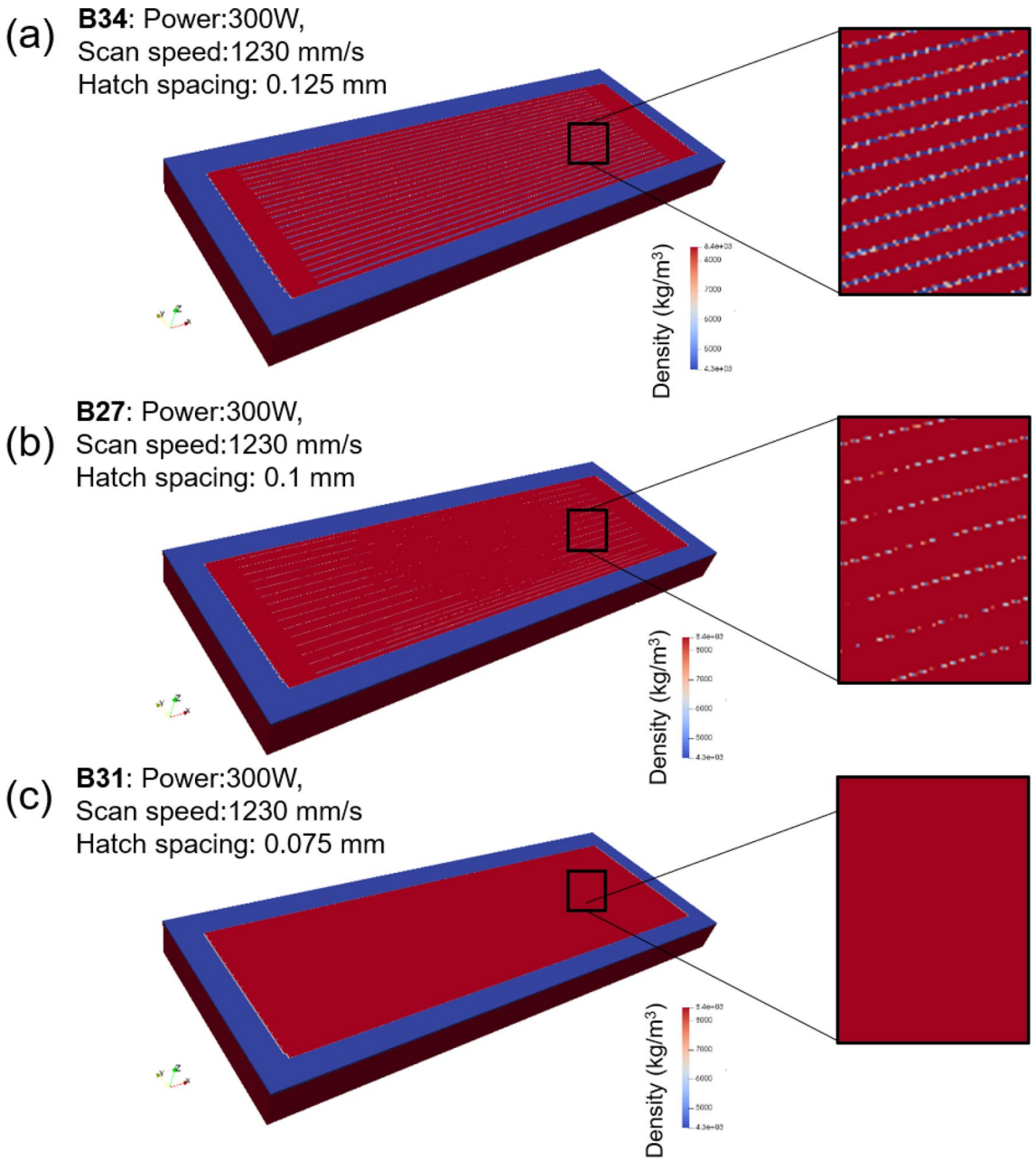

Fig. 15 Lack-of-fusion patterns for three cases. Magnification views are also shown to visualize the local lack-of-fusion patterns. **a** B34. **b** B27. **c** B31

Table 4 Computational parameters, mesh systems, and computational time for multi-track cases. All the simulations were conducted at Northwestern computer cluster "Ares." The in-house code (AM-CFD) was paralleled using OpenMP. Each simulation case ran on one cluster node that consists of two, 12-core Xeon E5-2680v3 2.5 GHz processors with 64 GB of memory

Case number	Mesh system	Size of scan region (mm)	Cells number	Physical time (ms)	Time step (μs)	Iterations number at each time step	Computational time (hour)
B26	Uniform	3*3	5.3 million	92	20	50	**17**
	Adaptive	3*3	0.66 million	92	20	50	**1.5 (*11x speedup*)**
B27	Uniform	10*3	15 million	271	20	50	**140**
	Adaptive	10*3	2 million	271	20	50	**13 (*11x speedup*)**
B31	Uniform	10*3	15 million	362	20	50	**168**
	Adaptive	10*3	2 million	362	20	50	**15 (*11x speedup*)**
B34	Uniform	10*3	15 million	217	20	50	**112**
	Adaptive	10*3	2 million	217	20	50	**10 (*11x speedup*)**
B35	Uniform	10*3	15 million	287	20	50	**140**
	Adaptive	10*3	2 million	287	20	50	**13 (*11x speedup*)**
B38	Uniform	15*3	21 million	511	20	50	**453**
	Adaptive	15*3	3 million	511	20	50	**45 (*10x speedup*)**

achieve an order of magnitude speedup as compared with the uniform mesh system.

Prediction and Validation of Multi-Layer Scans

Lastly, we simulated two thin-wall specimens, B21 and B25, consisting of 10 consecutive 40 μm thick layers each with a track length of 5 mm. Similar to the experiments, the laser moves in the same direction for each layer during the processes. Each case used a different laser power and scan speed as shown in Table 5. Figure 16a shows the simulated result for case B21. The as-built material is represented in red, while the substrate is colored blue. For a quantitative comparison, we divided the wall into three measurement zones shown in Fig. 16a, i.e., Zone 1: $x' = 0$ mm to $x' = 0.5$ mm, Zone 2: $x' = 0.5$ mm to $x' = 4.5$ mm, and Zone 3: $x' = 4.5$ mm to $x' = 5$ mm. The average and standard deviation of the height above the substrate pad datum and the total cross-sectional area for the entire portion of the wall above the substrate pad datum were measured for each measurement zone as shown in Fig. 16b. It should be noted that the cross-sectional area and the height were measured from cross sections collected approximately every 200 μm in each zone. There is a minimum of 3 cross sections collected within Zones 1 and 3, and approximately 20 cross sections in Zone 2. Figure 17 shows the comparisons of the height and cross-sectional area for the three different zones between the experimentally measured and computationally predicted

Table 5 Process parameters used for multi-layer cases

Case number	Laser power (W)	Scan speed (mm/s)	Layer thickness (μm)	Track length (mm)	The number of layers
B21	300	1230	40	5	10
B25	241	1529	40	5	10

results. The simulated height and area agree well with the measurements at Zone 2 and Zone 3, which indicates the developed model can predict the steady-state melt pool geometry well. However, at Zone 1, i.e., the beginning region of each layer, the model underestimates the results. This implies that some transient behaviors occurring at the beginning of each layer are being neglected by the model. More detailed analysis of the multi-layer experiments can be found in reference [22].

Conclusions

In this work, we proposed an integrated computational framework including physics-based modeling, data-driven calibration, and experimental validation. This framework was demonstrated for a systematic benchmark study of the L-PBF AM process for Inconel 625 material. Predicted results from the model were compared against experimental measurements from the AFRL AM Challenge Series of

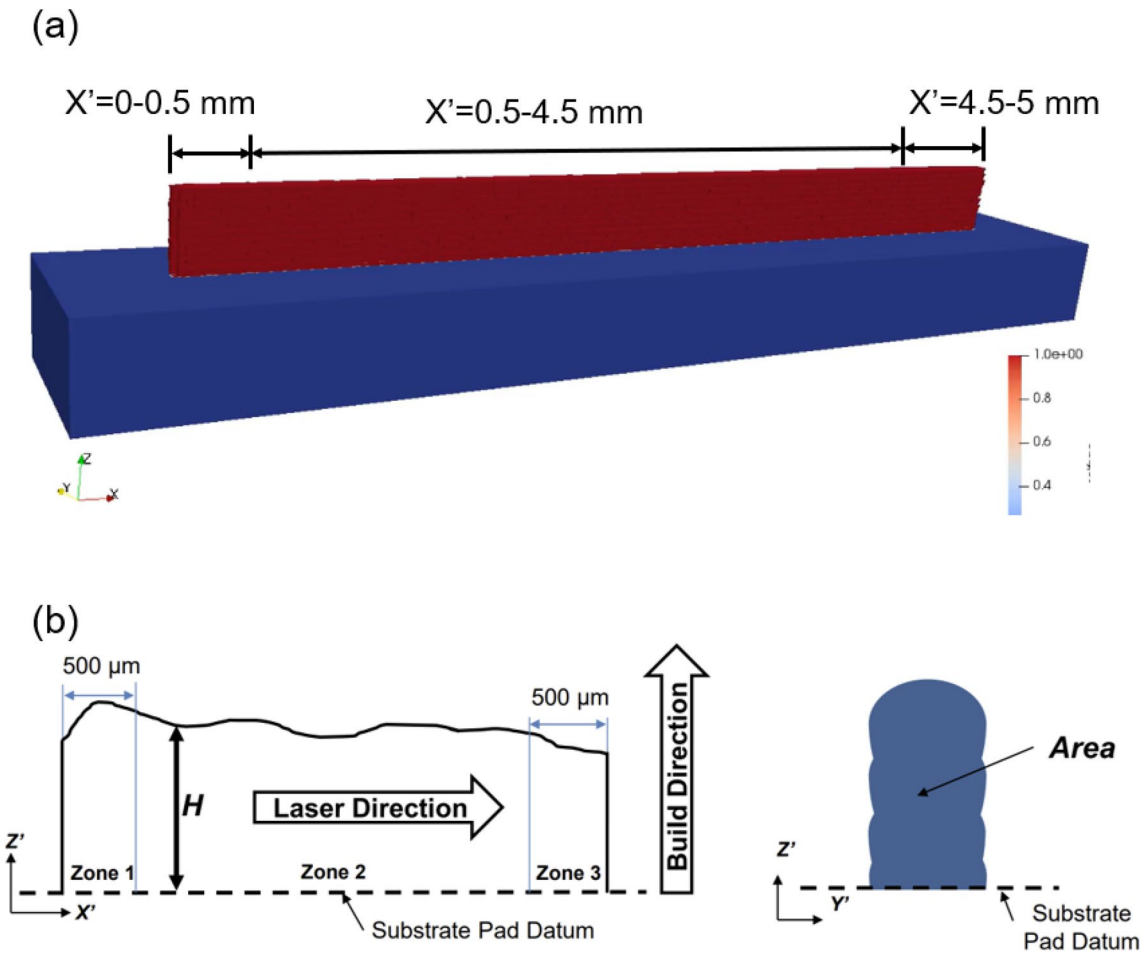

Fig. 16 As-built multi-layer structure and its measurements for case B21. **a** As-built material in red and substrate in blue. **b** A schematic of the height and cross-sectional area measurements for three Zones, i.e., Zone 1: $x' = 0$–0.5 mm, Zone 2: $x' = 0.5$–4.5 mm, and Zone 3: $x' = 4.5$–5 mm

melted track geometries for both single-layer single-track, single-layer multi-track, and multi-layer thin-wall builds. From these studies, we conclude:

1. With an appropriate calibration procedure using a small amount of experimental data, the proposed thermal-fluid model can quantitatively predict melted track geometries in multi-track and multi-layer L-PBF processes of Inconel 625 material.
2. The PGD-based calibration approach is robust and efficient even when using noisy AM experimental data.
3. The developed toolpath-based adaptive mesh strategy is effective for L-PBF computations, and can achieve a speedup of more than 10 times compared to a uniform mesh approach.
4. The residual heat factor (RHF) model can capture transient dynamics of the melt pool at the ends of the toolpath for multi-track AM process. The thermal-fluid model coupled with the RHF model has greater accuracy in predicting melted track geometries and patterns especially at the regions near the starting and ending points of the toolpath.
5. Dwell time between adjacent scan tracks is an important parameter that affects the uniformity of the melted track geometries. The simulation provides a way to analyze this phenomenon and reduce variability of the melt pool during the process.
6. The developed model has the capability to capture lack-of-fusion defect during the L-PBF process. It can potentially be used as an effective tool for mitigating lack-of-fusion porosity by optimizing the process parameters, although more validation studies are needed for testing the lack-of-fusion predictions in the future.
7. The developed model can predict the steady-state melt pool geometry well. However, the model underestimates the height and cross-sectional area at the beginning region of each layer for multi-layer AM process because some transient behaviors are not captured at the beginning of each layer by the model. Further enhanced transient modeling will be pursued in the future.

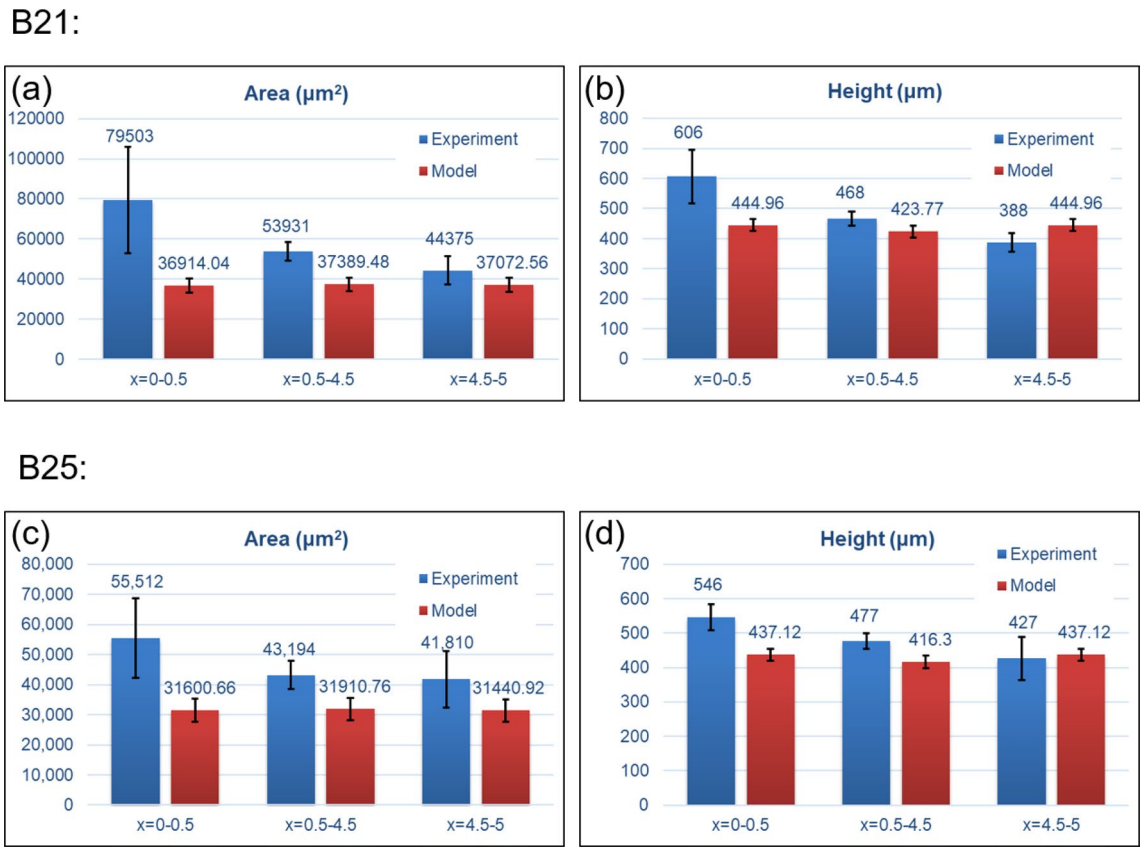

Fig. 17 Quantitative comparisons of height and cross-sectional area between experimental measurements and model predictions: **a** cross-sectional area for case B21, **b** height for case B21, **c** cross-sectional area for case B25, and **d** height for case B25

Supplementary Information The online version supplementary material is available at https://doi.org/10.1007/s40192-021-00209-4.

Acknowledgements W. K. Liu acknowledges the support by the Center for Hierarchical Materials Design (CHiMaD) under Grant No. 70NANB14H012 and NSF Grant CMMI-1934367. Z. Gan and Y. Lu acknowledge the partial support of NSF Grants CMMI-1934367 and 1762035. K. Jones acknowledges the support by the Murphy Fellowship from Northwestern University and NSF Grant CMMI-1934367. We extend our appreciation to Dr. Edwin Schwalbach, Marie Cox, and the AM Challenge Series committee for their work and leadership in providing this valuable forum for the AM research community.

Declarations

Conflict of interest On behalf of all authors, the corresponding author states that there is no conflict of interest

References

1. Bourell D, Beaman J, Marcus H, Barlow J (1990) Solid freeform fabrication: an advanced manufacturing approach. In: International solid freeform fabrication symposium, pp 1–7
2. Vojislav P, Juan VHG, Olga JF, Javier DG, Jose RBP, Luis PG (2011) Additive layered manufacturing: sectors of industrial application shown through case studies. Int J Prod Res 49:1061–1079
3. Yan C, Hussein A, Raymont D (2012) Evaluations of cellular lattice structures manufactured using selective laser melting. Int J Mach Tools Manuf 62:32–38
4. Guo N, Leu MC (2013) Additive manufacturing: technology, applications and research needs. Front Mech Eng 8:215–243
5. Bourell D, Leu M, Rosen D (2009) Roadmap for additive manufacturing-Identifying the future of freeform processing. The University of Texas at Austin, Laboratory for Freeform Fabrication, Advanced Manufacturing Center
6. Liu Y, Li S, Wang H, Hou W, Hao Y, Yang R, Sercombe T, Zhang L (2016) Microstructure, defects and mechanical behavior of beta-type titanium porous structures manufactured by electron beam melting and selective laser melting. Acta Mater 113:56–67
7. Witherell P, Feng SC, Martukanitz R, Simpson TW, John DB, Michaleris P, Liu Z-k, Chen L-q (2014) Toward metamodels for composable and reusable additive manufacturing process models. In: 34th computers and information in engineering conference, proceedings of the ASME design engineering technical conference, American Society of Mechanical Engineers (ASME), p 061025
8. Cunningham R, Narra SP, Montgomery C, Beuth J, Rollett AD (2017) Synchrotron-based x-ray microtomography characterization of the effect of processing variables on porosity formation in laser power-bed additive manufacturing of Ti-6Al-4V. JOM 69:479–484

9. Tang M, Postorius PC, Beuth JL (2017) Prediction of lack-of-fusion porosity for powder bed fusion. Addit Manuf 14:39–48
10. Smith J, Xiong W, Yan W, Lin S, Cheng P, Kafka OL, Wagner GJ, Cao J, Liu WK (2016) Linking process, structure, property, and performance for metal-based additive manufacturing: computational approaches with experimental support. Comput Mech 57:583–610
11. Gan Z, Liu H, Li S, He X, Yu G (2017) Modeling of thermal behavior and mass transport in multi-layer laser additive manufacturing of Ni-based alloy on cast iron. Int J Heat Mass Transf 111:709–722
12. Ghosh S, Ma L, Levine LE, Ricker RE, Stoudt MR, Heigel JC, Guyer JE (2018) Single-track melt-pool measurements and microstructures in inconel 625. JOM 70:1–6
13. Yan W, Lu Y, Jones K, Yang Z, Fox J, Witherell P, Wagner G, Liu WK (2020) Data-driven characterization of thermal models for powder-bed-fusion additive manufacturing. Addit Manuf 36:101503
14. Gan Z, Lian Y, Lin SE, Jones KK, Liu WK, Wagner GJ (2019) Benchmark study of thermal behavior, surface topography, and dendritic microstructure in selective laser melting of inconel 625. Integr Mater Manuf Innov 8:178–193
15. Heigel JC, Lane BM (2018) Measurement of the melt pool length during single scan tracks in a commercial laser powder bed fusion process. J Manuf Sci Eng 140:051012
16. Zhao C, Fezzaa K, Cunningham RW, Wen H, De Carlo F, Chen L, Rollett AD, Sun T (2017) Real-time monitoring of laser powder bed fusion process using high-speed x-ray imaging and diffraction. Sci Rep 7:3602
17. Fox JC, Lane BM, Yeung H (2017) Measurement of process dynamics through coaxially aligned high speed near-infrared imaging in laser powder bed fusion additive manufacturing. In: Bison P, Burleigh D (Eds.), Thermosense: thermal infrared applications XXXIX, volume 10214, International Society for Optics and Photonics, SPIE, pp 34–50. https://doi.org/10.1117/12.2263863
18. Lane B, Heigel J, Ricker R, Zhirnov I, Khromschenko V, Weaver J, Phan T, Stoudt M, Mekhontsev S, Levine L (2020) Measurements of melt pool geometry and cooling rates of individual laser traces on in625 bare plates. Integr Mater Manuf Innov 9:16–30
19. Heigel JC, Lane BM, Levine LE (2020) In situ measurements of melt-pool length and cooling rate during 3d builds of the metal AM-bench artifacts. Integr Mater Manuf Innov 9:31–53
20. America Makes (2019a) America makes and air force research laboratory announce an additive manufacturing modeling challenge series. https://www.americamakes.us/america-makes-and-afrl-announce-am-modeling-challenge/
21. America Makes (2019b) Air force research laboratory (AFRL) additive manufacturing modeling challenge series. https://www.americamakes.us/am-modeling-challenge-series/
22. Edwin MAG, Schwalbach J, Chapman Michael G (2021) AFRL additive manufacturing modeling series: challenge 2—microscale process to structure data description. In review
23. Lu Y, Blal N, Gravouil A (2018) Adaptive sparse grid based HOPGD: toward a nonintrusive strategy for constructing space-time welding computational vademecum. Int J Numer Methods Eng 114:1438–1461
24. Lu Y, Blal N, Gravouil A (2019) Datadriven HOPGD based computational vademecum for welding parameter identification. Comput Mech 64:47–62
25. Gan Z, Yu G, He X, Li S (2017) Numerical simulation of thermal behavior and multicomponent mass transfer in direct laser deposition of co-base alloy on steel. Int J Heat Mass Transf 104:28–38
26. Lian Y, Gan Z, Yu C, Kats D, Liu WK, Wagner GJ (2019) A cellular automaton finite volume method for microstructure evolution during additive manufacturing. Mater Des 169:107672
27. Ye J, Khairallah SA, Rubenchik AM, Crumb MF, Guss G, Belak J, Matthews MJ (2019) Energy coupling mechanisms and scaling behavior associated with laser powder bed fusion additive manufacturing. Adv Eng Mater 21:1900185
28. Fabbro R, Dal M, Peyre P, Coste F, Schneider M, Gunenthiram V (2018) Analysis and possible estimation of keyhole depths evolution, using laser operating parameters and material properties. J Laser Appl 30:032410
29. Capriccioli A, Frosi P (2009) Multipurpose ansys fe procedure for welding processes simulation. In: Fusion engineering and design 84 546–553. Proceeding of the 25th symposium on fusion technology
30. America Makes (2019) Air force research laboratory (AFRL) additive manufacturing modeling challenge series 2. https://materials-data-facility.github.io/MID3AS-AM-Challenge/Challenge2ProblemStatement_2019Release.pdf
31. Pawel R, Williams R (1985) Survey of physical property data for several alloys. Technical Report, Oak Ridge National Laboratory
32. Valencia JJ, Quested PN (2013) Thermophysical properties
33. Yeung H, Lane B (2020) A residual heat compensation based scan strategy for powder bed fusion additive manufacturing. Manuf Lett 25:56–59
34. Whitley D (1994) A genetic algorithm tutorial. Stat Comput 4:65–85
35. Lu Y, Blal N, Gravouil A (2018) Multi-parametric space-time computational vademecum for parametric studies: application to real time welding simulations. Finite Elements Anal Des 139:62–72
36. Lu Y, Blal N, Gravouil A (2018) Space-time pod based computational vademecums for parametric studies: application to thermo-mechanical problems. Adv Model Simul Eng Sci 5:1–27
37. Ammar A, Mokdad B, Chinesta F, Keunings R (2006) A new family of solvers for some classes of multidimensional partial differential equations encountered in kinetic theory modeling of complex fluids. J Nonnewton Fluid Mech 139:153–176
38. Néron D, Ladevèze P (2010) Proper generalized decomposition for multiscale and multiphysics problems. Arch Comput Methods Eng 17:351–372
39. Modesto D, Zlotnik S, Huerta A (2015) Proper generalized decomposition for parameterized helmholtz problems in heterogeneous and unbounded domains: Application to harbor agitation. Comput Methods Appl Mech Eng 295:127–149
40. Ghnatios C, Masson F, Huerta A, Leygue A, Cueto E, Chinesta F (2012) Proper generalized decomposition based dynamic data-driven control of thermal processes. Comput Methods Appl Mech Eng 213:29–41
41. Saha S, Kafka OL, Lu Y, Yu C, Liu WK (2021) Microscale structure to property prediction for additively manufactured in625 through advanced material model parameter identification. Integr Mater Manuf Innov. https://doi.org/10.1007/s40192-021-00208-5
42. Mukherjee T, Wei H, De A, DebRoy T (2018) Heat and fluid flow in additive manufacturing–part i: modeling of powder bed fusion. Comput Mater Sci 150:304–313
43. Martin AA, Calta NP, Khairallah SA, Wang J, Depond PJ, Fong AY, Thampy V, Guss GM, Kiss AM, Stone KH et al (2019) Dynamics of pore formation during laser powder bed fusion additive manufacturing. Nat Commun 10:1–10
44. Coeck S, Bisht M, Plas J, Verbist F (2019) Prediction of lack of fusion porosity in selective laser melting based on melt pool monitoring data. Addit Manuf 25:347–356
45. Yakout M, Elbestawi M, Veldhuis SC (2018) A study of thermal expansion coefficients and microstructure during selective laser melting of Invar 36 and stainless steel 316L. Addit Manuf 24:405–418